

# HI in and behind the Hubble Frontier Field Clusters: A Deep MeerKAT Pilot Search out to $z \sim 0.5$

Shilpa Ranchod<sup>1,2\*</sup>, Roger Deane<sup>1,2</sup>, Danail Obreschkow<sup>3</sup>, Tariq Blecher<sup>4</sup>, Ian Heywood<sup>4,5,6</sup>,

<sup>1</sup>*Department of Physics, University of Pretoria, Private Bag X20, Pretoria 0028, South Africa*

<sup>2</sup>*Wits Centre for Astrophysics, School of Physics, University of the Witwatersrand, 1 Jan Smuts Avenue, 2000, South Africa*

<sup>3</sup>*International Centre for Radio Astronomy Research (ICRAR), M468, University of Western Australia, WA 6009, Australia*

<sup>4</sup>*Department of Physics and Electronics, Rhodes University, PO Box 94, Makhanda 6140, Eastern Cape, South Africa*

<sup>5</sup>*Oxford Astrophysics, Denys Wilkinson Building, University of Oxford, Keble Rd, Oxford, OX1 3RH, UK*

<sup>6</sup>*South African Radio Astronomy Observatory, 2 Fir Street, Observatory, 7925, South Africa*

Accepted XXX. Received YYY; in original form ZZZ

## ABSTRACT

The Hubble Frontier Fields (HFF) are a selection of well-studied galaxy clusters used to probe dense environments and distant gravitationally lensed galaxies. We explore the 21cm neutral hydrogen (HI) content of galaxies in three of the HFF clusters, Abell 2744 ( $z = 0.308$ ), Abell S1063 ( $z = 0.346$ ) and Abell 370 ( $z = 0.375$ ), to investigate the evolution of gas in galaxies within intermediate redshift clusters. Using Early Science MeerKAT observations, we perform spectral-line stacking with HI cubes and make a  $3\sigma$  stacked detection for blue galaxies in Abell S1063 ( $M_{\text{HI}} = 1.22_{-0.36}^{+0.38} \times 10^{10} M_{\odot}$ ). We determine the  $3\sigma$  HI mass detection limits of Abell 2744 and Abell 370 to be at the knee of the HI Mass Function. A final, more ambitious objective of this work is to search for gravitationally lensed HI emission behind these clusters, enabled by MeerKAT’s wide instantaneous bandwidth. We find no evidence of highly magnified HI emission at  $0.33 < z < 0.58$ . The low thermal noise levels achieved in these pilot observations, despite short integration times, highlights the enormous potential of future MeerKAT HI observations of dense environments and the intermediate-redshift Universe.

**Key words:** galaxies: clusters: individual – radio lines: galaxies – instrumentation: interferometers

## 1 INTRODUCTION

Environment has been shown to play an important role in galaxy evolution. In dense environments, such as galaxy clusters and groups, galaxies are subject to a multitude of effects that can alter their morphology, gas and star-formation properties (e.g. Verheijen 2004; Dénes et al. 2015). A statistical result of this, the morphology-density relation (e.g. Dressler et al. 1997; van der Wel et al. 2010; Wetzel et al. 2013), shows that early-type (elliptical and lenticular) galaxies are preferably found in clusters, with the number of late-type (spiral and irregular) galaxies decreasing with environment density in the local Universe.

Galaxy clusters are the most massive virialised structures in the Universe and grow via the accretion of gas and galaxies along filaments in the cosmic web (e.g. Salerno et al. 2020). Within galaxy clusters, an important transformation mechanism is ram pressure stripping (Gunn & Gott 1972), where the gas of the interstellar medium (ISM) of an infalling galaxy is stripped by the intracluster medium (ICM, e.g. Vollmer et al. 2013; Sorgho et al. 2017; Ramatsoku et al. 2020). In addition to interactions with the ICM, cluster galaxies are subject to fast interactions with other cluster members, known as galaxy harassment (Moore et al. 1998; Bialas et al. 2015). These processes can result in gas being removed from galaxies, or rapidly increases the star-formation rate, which quickly depletes the

gas reservoir ( $\sim 10^7$  years, Poggianti et al. 2004). Because gas serves as the essential fuel for star-formation, these mechanisms are directly linked to the quenching of star-formation in the cluster environment, which results in the reddening of galaxies and the transformation of morphology (e.g. Odekon et al. 2016; Joshi et al. 2020).

A fundamental tool for studying these gas removal processes is the observation of neutral hydrogen (HI). HI makes up a large component of the ISM and can be directly observed via the 21 cm emission line. It has an important role in the baryon cycle, in which it is converted into H<sub>2</sub>, which fuels star-formation (Kereš et al. 2005; Obreschkow & Rawlings 2009; Péroux & Howk 2020). Within galaxies, HI is diffuse, and extends beyond the stellar component (e.g. Broeils & Rhee 1997; Leroy et al. 2008), making it a sensitive long dynamical tracer of the different environmental processes (e.g. Oosterloo & van Gorkom 2005; Serra et al. 2012; Saponara et al. 2017). It is crucial to study the HI content and distribution in cluster galaxies, to fully understand these mechanisms (e.g. Brown et al. 2016; Deshev et al. 2020). Such observations have shown that the effect of ram-pressure stripping is the strongest in the central regions of dense clusters, with evidence showing that the HI can be fully depleted after a galaxy has passed through the cluster centre (Roediger & Brüggner 2007). Observations of low-redshift clusters have shown unusual disruptions in the HI-discs of cluster galaxies, tidal features, and HI deficient galaxies (e.g. Solanes et al. 2001; Jaffé et al. 2015; Lee-Waddell et al. 2017; Gavazzi et al. 2018). Some galaxies are thought to go through environment-induced “pre-processing” before entering

\* E-mail: shilparanchod@gmail.com

a massive cluster environment (Li et al. 2020). The pre-processing takes place in low-mass groups in the form of galaxy-galaxy interactions and ram pressure stripping (Hess & Wilcots 2013; Jaffé et al. 2013, 2015), which typically reduces the H I content of these galaxies. Tracing the pre-processing is important for understanding the gas content of galaxies, and how this evolves with large-scale structure and over cosmic time.

H I has not been observed in detail beyond  $z = 0.2$ , due to the faintness of the H I emission line, with the record for the highest redshift direct H I emission detection of a single galaxy at  $z = 0.37$ , with  $M_{\text{HI}} = 2.9 \times 10^{10} M_{\odot}$  (Fernández et al. 2016). This galaxy resides beyond the knee of the HIMF and is therefore not representative of the general H I galaxy population at this redshift, however, statistical detections of intermediate redshift H I are possible. H I spectral stacking has been highly successful in quantifying the average H I content of large numbers of galaxies in the nearby Universe, and beyond  $z = 0.2$  (e.g. Delhaize et al. 2013; Rhee et al. 2013; Kanekar et al. 2016; Bera et al. 2019), with the most distant stacked H I detection at  $0.74 < z < 1.45$  for 7653 blue, star-forming galaxies (Chowdhury et al. 2020). With this technique, the average H I mass of a region (e.g. a galaxy cluster, group or blind field) is determined by co-adding the appropriately shifted spectra for a sample of galaxies in the region. H I spectral stacking has been successful in detecting the average H I in and around  $0.2 < z < 0.3$  galaxy clusters (Verheijen et al. 2007; Lah et al. 2009), and in the local Universe, has been used to probe the H I substructure of the Coma cluster (Healy et al. 2021).

In addition to being useful laboratories for studying the evolution of galaxies in dense environments, galaxy clusters can be effective gravitational lenses (for a review, see Kneib & Natarajan 2011). Gravitational lensing is the deflection of light by intervening mass, that can produce highly magnified and distorted images of background galaxies. The large mass and solid angle covered by highly concentrated galaxy clusters make them ideal gravitational lenses, which can be used as “cosmic telescopes” to observe very distant galaxies (e.g. Richard et al. 2009). The amplification of sources through gravitational lensing has been extremely effective in observing faint, distant sources across the electromagnetic spectrum, including continuum and spectral line emission in the radio domain (e.g. Carilli & Walter 2013, and references therein). While molecular gas has been studied across the Universe up to  $z \sim 1$  and beyond, H I emission remains undetected through lensing, with two searches for galaxy-galaxy lensed H I sources at  $z \sim 0.4$  (Hunt et al. 2016; Blecher et al. 2019). Gravitational lensing conserves surface brightness while increasing the solid angle of the source, boosting the observed flux. This amplification  $\mu$  can facilitate the detection of unresolved lensed sources, which maximises their detection probability, and reduces the integration time needed for a given source by  $\mu^2$ . Next-generation cm-wavelength interferometers are now sensitive enough to observe the higher redshift H I Universe, and the detection of gravitationally lensed H I is probable in new surveys (Deane et al. 2015). The detection of lensed H I behind intermediate-redshift galaxy clusters will provide a deep cosmic view of H I emission in galaxies, pre-SKA era, within a fraction of the observation time of unlensed detections. Successful lensed H I detections, along with readily detected CO emission lines, will constrain the H I/H<sub>2</sub> ratio at these redshifts, an important parameter in understanding galaxy evolution over cosmic time (Obreschkow & Rawlings 2009).

MeerKAT’s wide instantaneous bandwidth enables us to search for H I within intermediate-redshift galaxy clusters, and gravitationally lensed H I behind certain clusters in the L-band. Its large field of view makes it possible to observe these clusters with a single pointing and with shorter integration times than previous genera-

**Table 1.** Cluster properties. The far-right column only includes cluster members with spectroscopic redshifts.

	RA (J2000)	Dec (J2000)	$z$	$\sigma$ [km s <sup>-1</sup> ]	No. members
Abell 2744	00 <sup>h</sup> 14 <sup>m</sup> 21. <sup>s</sup> 2	-30°23′50.″1	0.308	1497 ± 47	167
Abell S1063	22 <sup>h</sup> 48 <sup>m</sup> 44. <sup>s</sup> 4	-44°31′48.″5	0.346	1840 <sup>+230</sup> <sub>-150</sub>	106
Abell 370	02 <sup>h</sup> 39 <sup>m</sup> 52. <sup>s</sup> 9	-01°34′36.″5	0.375	~ 1170	50

tion telescopes. Surveys such as LADUMA and MIGHTEE plan to detect H I emission up to a redshift of  $z \sim 0.58$  in the L-band and  $z \sim 1.4$  in the UHF-band (Jarvis et al. 2017; Blyth et al. 2016). Direct H I emission detections from these surveys are limited to high mass ( $M_{\text{HI}} > 10^{10} M_{\odot}$ ) galaxies beyond  $z \sim 0.35$ , with lower H I mass detections possible through statistical methods, such as stacking. The MeerKAT Galaxy Cluster Legacy Survey (MGCLS; Knowles et al. 2021), is the MeerKAT L-band survey of 115 galaxy clusters. This survey includes the observations of three of the Hubble Frontier Field (HFF) Clusters: Abell 2744, Abell S1063 and Abell 370 ( $0.3 < z < 0.4$ ). These massive clusters have strong lensing capabilities, which have been studied and modelled in detail with optical and infrared (OIR) observations (e.g. Jauzac et al. 2014; Mahler et al. 2017).

In this paper, we perform a deep search for H I emission in three of the southern/equatorial HFF clusters with MeerKAT, through direct detections and H I spectral stacking. In addition, we search for gravitationally lensed H I behind these clusters, up to  $z = 0.58$ . The paper is structured as follows. In Section 2 we describe the MeerKAT observations and data calibration strategy and summarise the ancillary data. In Section 3 we present the source-finding and stacking results. In Section 4 we show results for the lensed H I search. Section 5 is a discussion of the results, and a summary follows in Section 6.

Throughout this work we assume cosmological values of  $\Omega_M = 0.307$ ,  $\Omega_{\Lambda} = 0.691$  and  $H_0 = 67.7 \text{ km s}^{-1} \text{ Mpc}^{-1}$  (Planck Collaboration et al. 2015).

## 2 DATA

### 2.1 Hubble Frontier Field Clusters

Of the six HFF clusters, four are in the Southern/Equatorial sky and are therefore more conducive to deep, high fidelity imaging with MeerKAT. These clusters, namely Abell 2744, Abell S1063, Abell 370 and MACS J0416 are in the redshift range of  $0.3 < z < 0.4$ , and are some of the most massive clusters at these redshifts (Lotz et al. 2017). This range provides a balance between low-redshift, where clusters have low surface mass density, and high-redshift, where cluster mass has not significantly built up, as well as avoiding the redshift range with high RFI ( $0.1 < z < 0.3$ ). In addition, the cluster redshift range provides the optimal lensing efficiency for sources within the MeerKAT L- and UHF-bands. In this work, we observe Abell 2744, Abell S1063 and Abell 370, with plans for future observations of MACS J0416. The properties of the three observed clusters are summarised in Table 1 (e.g. Dressler et al. 1999; Owers et al. 2011; Williamson et al. 2011).

The HFF clusters have been well studied in a large range of wavelengths, including some of the deepest OIR observations of clusters (see Table 1), but have yet to be observed in H I emission, except for Abell 370 (Lah et al. 2009). Each cluster has an extensive suite of multi-wavelength catalogues (Shiple et al. 2018), including a fairly complete sample with spectroscopic redshifts (Owers et al. 2011; Karman et al. 2015; Mahler et al. 2017; Lagattuta et al. 2017). The

**Table 2.** Observation and Calibration Details for MeerKAT data

	Abell 2744	Abell S1063	Abell 370
RA (J2000)	00 <sup>h</sup> 14 <sup>m</sup> 19. <sup>s</sup> 51	22 <sup>h</sup> 48 <sup>m</sup> 43. <sup>s</sup> 50	02 <sup>h</sup> 39 <sup>m</sup> 50. <sup>s</sup> 50
Dec (J2000)	-30°23'19."20	-44°31'44."00	-01°35'08."00
Date	2018 July 5	2018 July 3	2019 June 16
Time range (UTC)	00:17 - 06:33	21:27 - 06:40	04:18 - 11:58
Number of antennas	61	61	62
Bandpass/flux calibrator	J0408-6545	J1939-6342	J0408-6545
Gain calibrator	J0025-2602	J2314-4455	J0323+0534
Time on target	6.27 hr	6.74 hr	7.27 hr
Processed frequency range	946–1092 MHz	856–1712 MHz	898–1423 MHz
Continuum Image size	5000 × 5000	10240 × 10240	10240 × 10240
Briggs weighting	0.0	-0.3	-0.3
Pixel Scale	2.0"	1.1"	1.1"
Restoring beam FWHM	9.8" × 8.7"	6.2" × 5.9"	8.1" × 6.1"
Image rms	9 μJy beam <sup>-1</sup>	3 μJy beam <sup>-1</sup>	5 μJy beam <sup>-1</sup>

precision of these redshift measurements is necessary for targeted HI surveys and statistical detection methods - i.e. stacking. The HFF clusters also have accurate mass models available from OIR lensing and X-ray analyses (e.g. Jauzac et al. 2014), an important tool needed to identify and model lensed HI detections.

## 2.2 MeerKAT Observations

The MeerKAT Galaxy Cluster Legacy Survey is a deep survey of 115 legacy galaxy clusters. The majority of observations make use of more than 60 antennas and consist of  $\sim 10$  hour integration times. The observations used the 4K correlator mode which has a channel width of 209 kHz, corresponding to  $44 \text{ km s}^{-1}$  at  $z = 0$ . The complex gain and bandpass calibrators, as well as additional information for each observation, are summarised in Table 2.

## 2.3 Calibration and Imaging

The MeerKAT data were calibrated (1GC and 2GC) and imaged using the OXKAT<sup>1</sup> (Heywood 2020) and CARACAL<sup>2</sup> (Józsa et al. 2020) pipelines. OXKAT is composed of a suite of packages, including CASA (McMullin et al. 2007), WSCLEAN (Offringa et al. 2014) and the TRICOLOUR<sup>3</sup> flagging software. The OXKAT scripts were run within SINGULARITY containers on the ILIFU Cloud facility<sup>4</sup>, and the pipeline follows a standard calibration strategy. Briefly, the calibration process is as follows:

(i) **1GC:** Basic flagging is applied to the calibrator fields, and auto-flagging on model-subtracted calibrators. These flags are then applied to the target. Flux, delay, bandpass and gain calibrations are derived and applied iteratively, with rounds of flagging in between. The target data are split out of the Measurement Set. These tasks are executed with CASA, and diagnostic visibility plots are generated with RAGAVI<sup>5</sup> (Radio Astronomy Gains And Visibility Inspector) and SHADEMS<sup>6</sup>, a tool for plotting interferometric visibilities.

(ii) **Imaging:** The target data are flagged using TRICOLOUR, and imaged using WSCLEAN. The initial imaging run is blind and shallow, with imaging parameters as summarised in Table 2. A deconvolution mask is then created from the image using local RMS thresholding.

(iii) **2GC:** Masked deconvolution is performed using WSCLEAN, from which model visibilities are predicted using WSCLEAN. One round of phase-only self-calibration is executed using CASA tasks<sup>7</sup>, and the result is imaged using WSCLEAN. Imaging parameters are summarised in Table 2.

Since this work began in the early stages of MeerKAT science verification, multiple approaches were used for calibration. CARACAL is a radio calibration pipeline that makes use of the STIMELA<sup>8</sup> (Makhathini 2018) scripting framework. STIMELA is a Python- and container-based framework that allows users to execute tasks from different radio calibration software packages using a single configuration file. These packages include CASA, MEQTREES<sup>9</sup> (Noordam & Smirnov 2010), and SoFIA (Serra et al. 2015), among others. CARACAL was also run on the ILIFU Cloud facility. The calibration strategy is as follows:

(i) **1GC:** Before cross-calibration, basic flagging on auto-correlations are applied to all fields using the CASA task `flagdata`, and autoflagging of RFI is done using AOFLAGGER (Offringa 2010). As done with OXKAT, flux, delay, bandpass and gain calibrations are derived and applied iteratively, with rounds of flagging in between, using CASA, and the target data were split out of the MS.

(ii) **Flagging:** The target MS is autoflagged with AOFLAGGER, using a custom flagging strategy.

(iii) **Imaging and 2GC:** This pipeline produces five images using WSCLEAN, with four rounds of self-calibration using CUBICAL<sup>10</sup> (Kenyon et al. 2018). The WSCLEAN auto-mask and auto-threshold parameters range from 20 to 5, and 0.5 to 0.3 respectively, decreasing with iterations. The other imaging parameters are summarised in Table 2. The first three rounds of self-calibration are phase-only, and the final round calibrates both phase and amplitude.

The data for Abell 2744 were calibrated using CARACAL, and Abell S1063 and Abell 370 were calibrated using OXKAT. For Abell 370, we did an additional round of manual flagging of short baselines ( $< 300\text{m}$ ) before 1GC using AOFLAGGER, following inspection.

After assessing that the quality of the calibration was satisfactory for HI imaging, the model visibilities were subtracted using CASA's `uvsub` task. For each cluster, spectral line imaging was performed for all the channels with frequencies corresponding to the redshift of the cluster and behind the cluster up to  $z < 0.5$ . The low-frequency end of the L-band (full bandwidth extent corresponds to  $z < 0.58$ ) was omitted, due to high RFI contamination at these frequencies. The Briggs robust weighting parameter was chosen for maximum sensitivity to faint emission. 'Cluster' cubes of  $\sim 100$  channels were constructed, centred around each cluster frequency, with channel widths corresponding to  $\sim 60 \text{ km s}^{-1}$  at  $z = 0.35$  and 'background' cubes were generated for lower frequencies corresponding up to  $z < 0.5$ . The selected frequency ranges for each cluster and the imaging parameters, along with the resultant cube PSF and rms values are summarised in Table 3. The CASA task `imcontsub` was used to remove residual continuum emission by subtracting a first or second-order polynomial from the spectral axis of the HI cubes. Although the targeted frequency ranges corresponding to the cluster

<sup>1</sup> <https://github.com/IanHeywood/oxkat>

<sup>2</sup> <https://github.com/caracal-pipeline/caracal>

<sup>3</sup> <https://github.com/ska-sa/tricolour>

<sup>4</sup> <http://www.ilifu.ac.za/>

<sup>5</sup> <https://github.com/ratt-ru/ragavi/>

<sup>6</sup> <https://github.com/ratt-ru/shadeMS>

<sup>7</sup> A more recent version of OXKAT now uses CUBICAL (Kenyon et al. 2018) and performs phase and delay self-calibration.

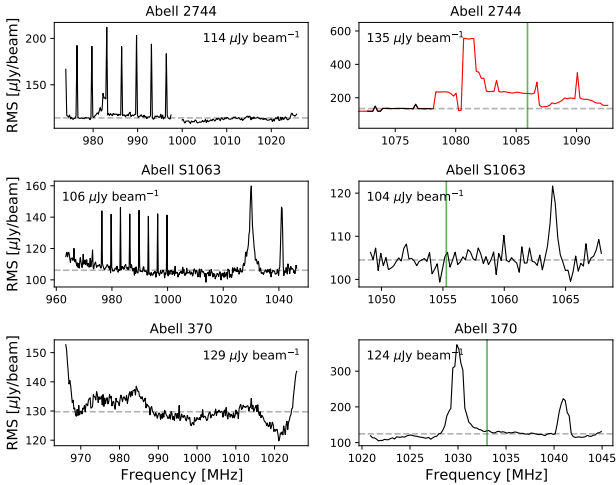
<sup>8</sup> <https://github.com/ratt-ru/Stimela>

<sup>9</sup> <https://github.com/ska-sa/meqtrees>

<sup>10</sup> <https://github.com/ratt-ru/CubiCal>

**Table 3.** H I cube imaging parameters and cube properties.

	Abell 2744	Abell S1063	Abell 370
<b>Cluster cube:</b>			
Cube frequency range	1072 – 1078 MHz	1049 – 1068 MHz	1020 – 1045 MHz
Cube redshift range	0.300 – 0.317	0.329 – 0.354	0.359 – 0.392
Cube velocity range	72318 - 73585 km s <sup>-1</sup>	74430 - 78443 km s <sup>-1</sup>	79288 - 84568 km s <sup>-1</sup>
Image size (pixels)	1000 × 1000	1000 × 1000	2800 × 2800
Image size (Mpc)	8.7 × 8.7	9.0 × 9.0	9.6 × 9.6
Pixel scale	2.0"	2.0"	2.5"
Briggs weighting	0.5	0.5	0.5
Restoring beam FWHM	17.0" × 11.3"	14.8" × 12.7"	23.6" × 13.2"
Median channel map rms	112 μJy beam <sup>-1</sup>	107 μJy beam <sup>-1</sup>	124 μJy beam <sup>-1</sup>
<b>Background cube:</b>			
Cube frequency range	974-1026 MHz	963-1046 MHz	966-1022 MHz
Cube redshift range	0.385 - 0.459	0.357 - 0.474	0.390 - 0.470
Image size (pixels)	1000 × 1000	1000 × 1000	2800 × 2800
Max image size (Mpc)	10.2 × 10.2	10.9 × 10.9	10.8 × 10.8
Pixel scale	2.0"	2.0"	2.5"
Briggs weighting	0.5	0.5	0.5
Restoring beam FWHM	17.3" × 11.7"	15.4" × 13.5"	22.6" × 12.6"
Median cube rms	113 μJy beam <sup>-1</sup>	110 μJy beam <sup>-1</sup>	129 μJy beam <sup>-1</sup>

**Figure 1.** The channel rms for the background cubes (left) and cluster cubes (right) for each cluster. The median rms is indicated on the plot and shown by the dashed horizontal line. The green vertical line shows the frequency corresponding to the cluster redshift. The red region for the Abell 2744 cluster cube indicates the frequency range that was excluded.

redshifts are mostly clear of RFI, there is particularly bad RFI contamination in the H I cube of Abell 2744. Fig. 1 shows the cube rms as a function of frequency, demonstrating that the majority of the cluster redshift range is contaminated. Because of this, we create a subcube of only 27 channels for this cluster (see Table 3).

In Fig. 1, there are noticeable periodic single-channel spikes in the cube rms, throughout the majority of the bandwidth of the Abell 2744 and Abell S1063 cubes. The spikes occur every 16 channels and are attributed to a firmware issue within the MeerKAT correlators at the time of observation, which was within the science verification stage of MeerKAT. In the cases where this is particularly severe, we have flagged the affected channels. The correlator issue was rectified before the observation of Abell 370 and does therefore not affect that observation.

## 2.4 Ancillary Data

The ancillary data used in this work are primarily from The Hubble Frontier Fields Programme catalogues (Shipley et al. 2018). This catalogue combines data from the *Spitzer* and the *Hubble Space Telescopes*. The optical *HST* observations were obtained using the Advanced Camera for Surveys WFC detector (ACS/WFC), and the near-IR observations were obtained using the Wide Field Camera 3 IR detector (WFC3/IR). These observations were conducted over 7 wide bands, over a wavelength range of 0.35 – 1.7 μm. Photometric redshifts were derived from the photometry, as described in Shipley et al. (2018), and spectroscopic redshifts were compiled from the literature, where available (Owers et al. 2011; Karman et al. 2015; Mahler et al. 2017; Lagattuta et al. 2017). The photometric and spectroscopic redshift distributions, for the catalogue objects in each cluster, are plotted in Fig. 2. The grey areas in Fig. 2 indicate frequencies with high RFI occupancy due to Global Positioning System (GPS) satellites and Global System for Mobile Communications (GSM) networks. Multiple < 1 MHz bandwidth intermittent RFI signals from 1000-1200 MHz (0.18 < z < 0.42), not indicated on the plot, may be present due to aircraft transponders.

A sub-catalogue of cluster members was compiled for each cluster. Following Ma et al. (2008), cluster membership is assigned to sources that have spectroscopic redshifts in the range of  $z = z_{cl} \pm 2.5\sigma$ , where  $z_{cl}$  is the mean cluster redshift, and  $\sigma$  is the velocity dispersion measured from Fig. 2. The number of cluster members for each cluster are listed in Table 1. Another sub-catalogue was created for target lensed sources. Sources were selected if they had a spectroscopic redshift greater than the maximum cluster redshift, as indicated in Fig. 2, and less than  $z \leq 0.5$ . Magnification maps for the HFF clusters have been modelled by multiple independent groups. Shipley et al. (2018) derive magnification values for each catalogue source from each group’s most recent model. In this work, we use the CATS (Clusters As TelescopeS, P.I. Ebeling, e.g. Jauzac et al. 2014) lensing models (Version 4.0), and the magnifications derived therefrom.



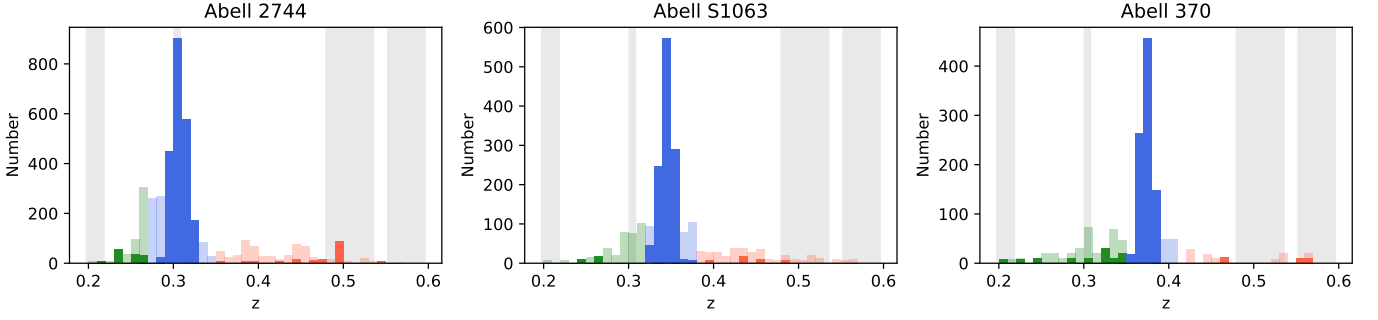


**Figure 2.** The stellar mass-weighted redshift distribution of objects in the HFF catalogues in the range of  $0 < z < 0.58$ . The blue represents the galaxies in the cluster redshift range, the green and red represent the objects in the cluster foreground and background respectively, with bin widths of  $z = 0.02$ . The high opacity bars show the sources with spectroscopic redshifts, and the low opacity bars show the objects that only have a photometric redshift. The grey areas indicate frequencies with high RFI occupancy.

### 3 CLUSTER H I

#### 3.1 Source Finding

Following a visual inspection with no direct H I detections, we performed a blind search for direct H I detections in the cluster cubes using SoFIA (Serra et al. 2015), a software package designed for 3D source-finding in large spectral line cubes. The following SoFIA strategy was used: A low threshold of  $2\sigma$  was selected for the Smooth + Clip algorithm. 3D boxcar smoothing kernels were used, with spatial dimensions of 5, 8 and 10 pixels (i.e. [10, 16, 20] arcsec, which corresponds to [46, 73, 92] kpc at  $z = 0.35$ ), and spectral dimensions of 1 and 2 channels. These dimensions were chosen to correspond to the expected velocity width for H I-massive and/or lensed galaxies, and the PSF FWHM of the cube. Pixels above the detection threshold were assigned to belong to the same source if they had a maximum separation of 2 spatial pixels or 2 frequency channels.

Using SoFIA’s reliability calculation, and assuming a reliability threshold of 0.95, no reliable detections were identified for any of the clusters. Assuming the median rms values listed in Table 3, we determined the  $5\sigma$  H I mass detection limit to be  $M_{\text{HI}} = 2.06 \times 10^{10} M_{\odot}$  for Abell 2744,  $M_{\text{HI}} = 1.94 \times 10^{10} M_{\odot}$  for Abell S1063 and  $M_{\text{HI}} = 2.31 \times 10^{10} M_{\odot}$  for Abell 370. Three candidate galaxies in Abell S1063 and one in Abell 370 have predicted H I masses greater than this limit, as estimated from the following equation from Meyer et al. (2017):

$$\left(\frac{S}{\text{JyHz}}\right) = \frac{1}{49.7} \left(\frac{M_{\text{HI}}}{M_{\odot}}\right) \left(\frac{D_L}{\text{Mpc}}\right)^{-2}, \quad (1)$$

and the  $M_{*} - M_{\text{HI}}$  relation from Parkash et al. (2018)

$$\log M_{\text{HI}} = 0.51(\log M_{*} - 10) + 9.71. \quad (2)$$

This relation has a scatter of 0.5 dex, so not all galaxies are guaranteed to be detected.

#### 3.2 H I Spectral Stacking

We use image domain spectral line stacking for sources with spectroscopic redshifts in each cluster. At this angular resolution, sources are not expected to be resolved e.g. a mean PSF FWHM of 15 arcsec is equal to 62 kpc at  $z = 0.3$ . The typical predicted diameter for sources in this sample is  $\sim 30$  kpc (Wang et al. 2016), with high mass outliers at  $\sim 80$  kpc. Note that sources with redshifts corresponding to fully flagged channels are removed before stacking. The spectra are shifted to rest-frame and a wrapping technique is implemented

(e.g. Healy et al. 2019), such that the original spectrum length is maintained. The flux spectra are converted to mass spectra using the following equation (e.g. Delhaize et al. 2013; Hu et al. 2019):

$$m_{\text{HI}}(\nu) = 4.97 \times 10^7 S_{\nu} D_L^2 f^{-1}. \quad (3)$$

Here,  $m_{\text{HI}}$  has units of  $M_{\odot} \text{MHz}^{-1}$ ,  $S_{\nu}$  is the rest-frame H I flux density in Jy,  $D_L$  is the luminosity distance in Mpc, and  $f$  is the normalised primary beam response. For MeerKAT, the primary beam has an FWHM of  $\sim 80'$  for H I at  $z = 0.3$  (Mauch et al. 2020), and the clusters have a maximum virial radius of  $\sim 3'$  from the centre of the primary beam. Because the entire cluster resides well within the centre of the primary beam, we can approximate the beam pattern as a Gaussian function in all target directions that is constant as a function of frequency.

For stacking, a weight function is introduced, following the procedure used by Hu et al. (2019), depending on the rms noise of individual spectra  $\sigma$ , the primary beam response  $f$ , and the luminosity distance  $D_L$ . The weight of the  $i^{\text{th}}$  galaxy is:

$$w_i = f^2 D_L^{-\gamma} \sigma^{-2}, \quad (4)$$

where large values of  $\gamma$  give more weight to nearby galaxies and small values of  $\gamma$  increase the statistical contribution of more distant galaxies. Hu et al. (2019) conclude that an optimal stacked SNR is achieved with  $\gamma = 1$ . It should be noted that in general,  $\gamma = 1$  is not necessarily the best choice for constraining average mass. However, since we cover a small redshift range, and a large SNR is essential, we choose  $\gamma = 1$ . The average stacked mass spectrum is calculated from the following equation:

$$\langle m_{\text{HI}}(\nu) \rangle = \frac{\sum_{i=1}^n w_i m_{\text{HI},i}}{\sum_{i=1}^n w_i}. \quad (5)$$

The integrated H I mass  $\langle M_{\text{HI}} \rangle$  is the integral of the spectral peak along the frequency axis:

$$M_{\text{HI}} = \int_{\nu_0 - \Delta\nu}^{\nu_0 + \Delta\nu} \langle m_{\text{HI}}(\nu) \rangle d\nu, \quad (6)$$

where  $\nu_0$  is the rest frequency of neutral hydrogen. A boxcar function is fit to the peak at rest frequency to estimate  $M_{\text{HI}}$  using Bayesian parameter estimation (see Section 3.2.4).

Each spectrum is smoothed with a Hanning function in frequency space, with a window of a specified width. Spatial smoothing is also implemented using CASA’s `imsmooth`. The smoothing kernel is well-matched to the intrinsic spatial ( $1.5 \times \text{PSF FWHM}$ ) and velocity ( $4$  channels or  $\sim 240 \text{ km s}^{-1}$ ) extent of the targeted sources.

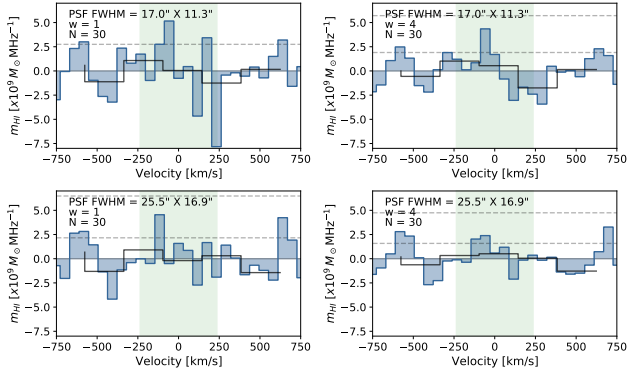


**Figure 3.** The stacked mass spectra for 30 galaxies with spectroscopic redshifts in Abell 2744. The plots are spatially and spectrally smoothed, as described in Section 3.2. The smoothed PSF dimensions, spectral smoothing window  $w$  in units of channel, and the number of spectra stacked  $N$  are shown in the top left corner. The black line shows the spectrum regridded to a velocity resolution of  $240 \text{ km s}^{-1}$ . The green region indicates the velocity range where we expect to detect H I emission for galaxies of this stellar mass, and the  $1\sigma$  and  $3\sigma$  H I mass rms are indicated by the grey dashed lines.

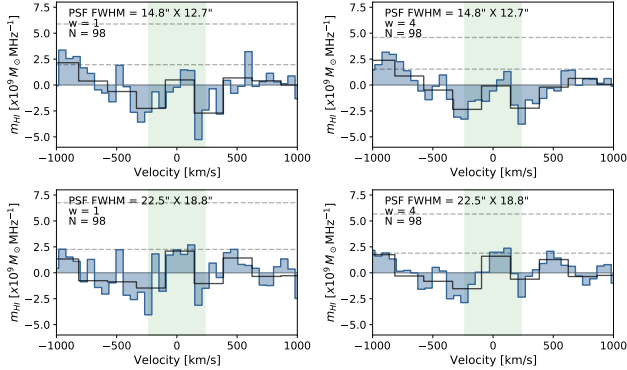


**Figure 4.** The stacked mass spectra for 98 galaxies with spectroscopic redshifts in Abell S1063, as in Fig. 3.

This stacking procedure was applied to four cubes for each cluster, with varying degrees and types of smoothing:

- (i) unsmoothed,
- (ii) spatially-smoothed,
- (iii) spectrally-smoothed, and
- (iv) spatially- and spectrally-smoothed

We also show the stacked spectra regridded to a velocity resolution of  $\sim 240 \text{ km s}^{-1}$ . The stacking results for all cluster members with spectroscopic redshifts are shown in Figs. 3, 4 and 5. The rms of the stacked spectra decreases as approximately  $\propto 1/\sqrt{N}$ , as expected for Gaussian noise, where  $N$  is the number of spectra stacked, for all three cubes.

These spectra show that there are no stacked H I detections in Abell 2744, Abell S1063, and Abell 370, for all cluster members with spectroscopic redshifts. For Abell 2744, the rms of the unsmoothed stacked spectrum corresponds to  $\sigma = 18 \mu\text{Jy beam}^{-1}$ , and we determine the  $5\sigma$  stacked H I mass detection limit to be  $M_{\text{HI}} = 2.89 \pm 0.21 \times 10^9 M_{\odot}$ , well below the knee of the HIMF. For Abell S1063 and Abell 370, we determine the  $5\sigma$  stacked H I mass detection limits to be  $M_{\text{HI}} = 2.05 \pm 0.04 \times 10^9 M_{\odot}$  ( $\sigma = 11 \mu\text{Jy beam}^{-1}$ ), and  $M_{\text{HI}} = 4.89 \pm 0.19 \times 10^9 M_{\odot}$  ( $\sigma = 15 \mu\text{Jy beam}^{-1}$ ),

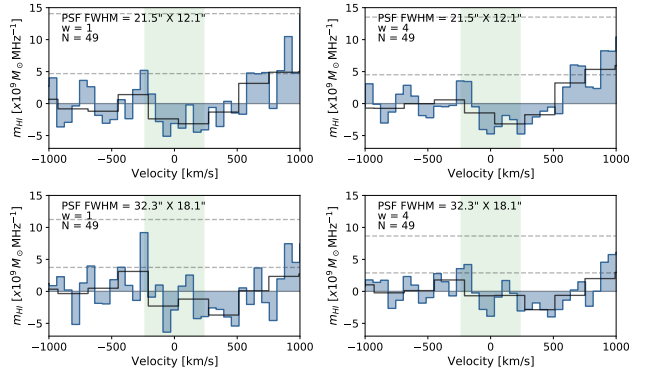


**Figure 5.** The stacked mass spectra for 49 galaxies with spectroscopic redshifts in Abell 370, as in Fig. 3.

respectively. Here, the rms has been converted to flux using Equation 3, for convenience. The uncertainties are calculated using jackknife resampling with  $(N - 1)$  samples, where  $N$  is the number of stacked spectra.

### 3.2.1 H I Deficiency

By comparing the predicted H I mass values for each cluster stack to H I detection mass limits, we can determine the H I deficiency parameter  $\text{DEF}_{\text{HI}}$ , first introduced by Haynes & Giovanelli (1984). This parameter is defined as

$$\text{DEF}_{\text{HI}} = \log_{10} \left( \frac{M_{\text{HI,exp}}}{M_{\odot}} \right) - \log_{10} \left( \frac{M_{\text{HI,obs}}}{M_{\odot}} \right), \quad (7)$$

where  $M_{\text{HI,exp}}$  and  $M_{\text{HI,obs}}$  are the expected and observed H I masses, respectively. We predict the expected stacked H I masses using Equation 2, assuming a velocity width of  $200 \text{ km s}^{-1}$  and the cube rms levels. While this relation may not hold or be accurate out to these redshifts and in these environments, it does provide a useful comparison. We find mean H I deficiency limits of galaxies in the respective clusters to be  $\text{DEF}_{\text{HI}} > 0.71 \pm 0.50$  for Abell 2744,  $\text{DEF}_{\text{HI}} > 0.57 \pm 0.50$  for Abell S1063, and  $\text{DEF}_{\text{HI}} > 0.33 \pm 0.50$  for Abell 370. The uncertainties are from the intrinsic scatter of the  $M_{*} - M_{\text{HI}}$  relation. These values for Abell 2744 and Abell S1063 fall above  $\text{DEF}_{\text{HI}} > 0.5$ . Therefore, following the Cortese et al. (2011) terminology, the galaxies in these clusters can, on average, be classified as H I deficient with respect to the main sequence of star-formation. The deficiency parameter for Abell 370 falls within the ‘H I normal’ limits of  $-0.5 < \text{DEF}_{\text{HI}} < 0.5$ . However, it should be noted that  $\text{DEF}_{\text{HI}} > 0.33$  is closer to the H I deficient boundary, and these values are lower limits, with large uncertainties. It is therefore likely that the galaxies in Abell 370 are also, on average, H I deficient. In addition, we should be mindful of the caveat that Equation 2 is typically applied to samples with a pre-selection of H I-rich, star-forming galaxies. Deeper observations and further H I emission detections are required for a better constraint on these values.

### 3.2.2 Blue Galaxies

Optically blue, star-forming galaxies typically have higher H I fractions than red, quiescent galaxies (e.g. Cortese et al. 2011; Brown et al. 2015). It has been found that stacking only blue galaxies results in higher SNR stacked detections when compared to stacking the full sample (e.g. Kanekar et al. 2016; Bera et al. 2019), which is

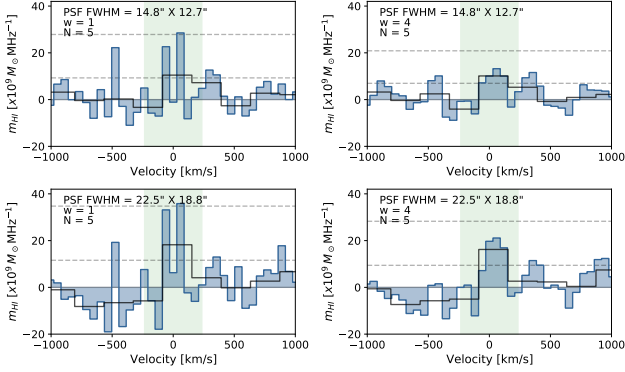


**Figure 6.** The stacked mass spectra for 5 blue galaxies with spectroscopic redshifts in Abell S1063, as in Fig. 3. The grey dashed lines show the 1 and  $3\sigma$  rms.

indicative of higher gas content in this sub-population. We determine the number of blue galaxies in each cluster sample using the colour-magnitude diagram, classifying sources as blue for  $(b - v) < 1$ , based on the separation from the red sequence for this statistically small sample. While this is not consistent with typical classifications in other analyses, it has achieved our objective in selecting the bluest of the sample. Of the cluster members with spectroscopic redshifts, we find the following: Abell 2744 has 7 blue galaxies, and Abell 370 has 3 blue galaxies, all of which do not fall in the redshift range of the limited subcube or are at fully flagged frequencies. Abell S1063 has 5 blue galaxies, all of which fall into the cluster cube frequency range. The stacked spectrum of these galaxies is shown in Fig. 6.

We make what appears to be a  $3\sigma$  stacked detection for blue galaxies in Abell S1063. This peak is visible at all shown degrees of smoothing but is significantly boosted for the spatially smoothed cube. We explore the purported detection in the following sections.

### 3.2.3 Proximity of Sources

Four of the five blue galaxies in Abell S1063 are located within  $30''$  (corresponding to 135 kpc in projection at  $z = 0.34$ ), and  $67 \text{ km s}^{-1}$  of one another. The coordinates of these sources are overlaid on the MeerKAT channel map corresponding to the median redshift of  $z = 0.3421$  (Fig. 7). To place this proximity into perspective with the cluster members as a whole, we plot the distribution of both the spatial and recession velocity separations between all galaxy pairs in the sample. We indicate the separation between the four nearby blue galaxies (i.e. the separation between six pairs of galaxies) on the full sample distributions in Fig. 8. As expected, we find that the spatial and velocity separation between the blue galaxies is below the modal separation of the sample. This, and the fact that four of the blue galaxies are heavily clustered near the virial radius of Abell S1063 strongly suggests that this is a recently in-fallen group (e.g. Jaffé et al. 2015). Despite the proximity of the four sources, we do not observe any obvious tidal features in the HFF images that would suggest ongoing merger activity.

### 3.2.4 Veracity of Stacked Detection

We test the veracity of this  $3\sigma$  detection to rule out the possibility of the peak being caused by the covariance of local image-plane noise. We do this by stacking five randomly selected spectra centred at  $z = 0.3421$ , that have the same relative separation of the blue galaxies.

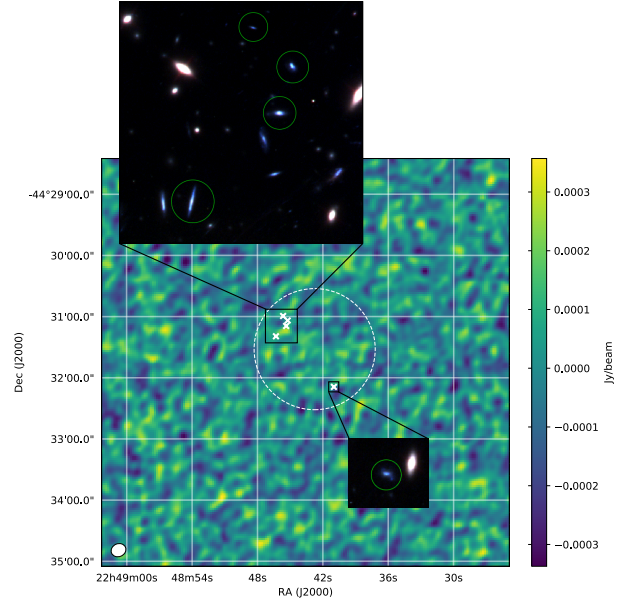


**Figure 7.** MeerKAT channel map of Abell S1063 corresponding to  $z = 0.3421$ . The white crosses indicate the positions of the 5 blue galaxies, and the dashed ellipse shows the approximate virial radius of the cluster. The restoring beam is shown in the bottom left. The insets show the RGB *HST* images of the indicated regions. The stacked sources are indicated by the green circles.

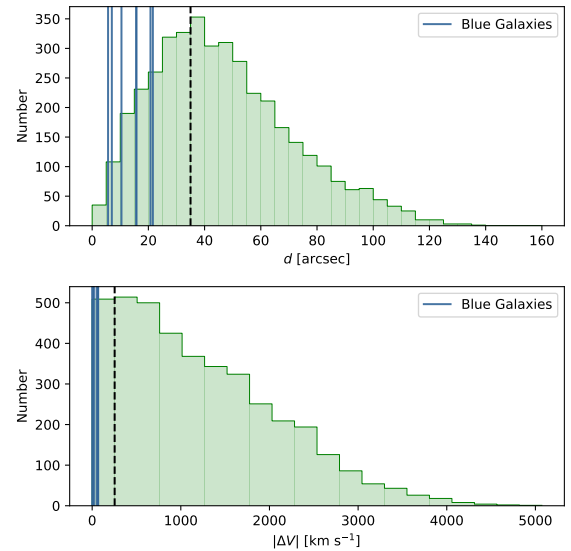


**Figure 8.** Histogram distribution of the projected spatial (top) and recession velocity (bottom) separation between all HFF galaxies in Abell S1063 (green). The separations between the four nearby blue galaxies are shown in blue. The dashed lines indicate the modal spatial separation and velocity.

These coordinates are drawn from a uniformly random distribution, within the spatial extent of the H I cube. The result of 100 random sets of stacked spectra is shown in Fig. 9 (grey lines). We find that none of these random realisations generates a stacked signal greater in significance than the data spectrum in the  $v = \pm 200 \text{ km s}^{-1}$  range, further strengthening the veracity of the detection. In addition, it is encouraging that the standard deviation of the random realisations is

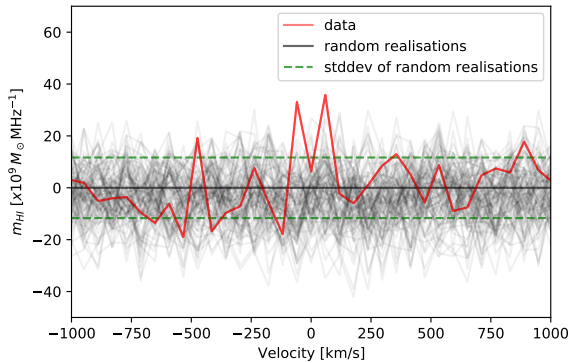


**Figure 9.** 100 random realisations of 5 stacked spectra (black), centred at  $z = 0.3421$  in Abell S1063. The positions of the five extracted spectra for each randomisation follows the same separation of the blue galaxies as shown in Fig. 7. The spectra have been extracted from a spatially smoothed cube, and the stacked spectrum for the blue galaxies is shown in red (as in the bottom left in Fig. 6). The green dashed line indicates the standard deviation of the random realisations.

similar to the  $1\sigma$  of the stacked spectrum, showing the Gaussianity of the noise.

As a further test of the robustness of the apparent stacked detection, we utilise a Bayesian framework for parameter estimation. To do so, we use a boxcar function whose width and height are expressed in terms of  $w_{50}$  and  $M_{\text{HI}}$ . This function has the favourable property of retaining the velocity for Gaussian and double-horned intrinsic spectra. The posteriors of these two model parameters are sampled using a Markov Chain Monte Carlo (MCMC) algorithm, with uniform priors. Assuming this boxcar model, we find the maximum likelihood estimates to be  $M_{\text{HI}} = 1.22^{+0.38}_{-0.36} \times 10^{10} M_{\odot}$  and  $w_{50} = 181^{+68}_{-11} \text{ km s}^{-1}$ , where the sub- and super-script values denote the 16<sup>th</sup> and 84<sup>th</sup> percentiles of the posterior distributions shown in Fig. 10. These distributions are consistent with the estimated  $3\sigma$  significance of the possible detection. This value is significantly larger than the predicted mean H I mass of the five sources,  $M_{\text{HI}} = 0.10^{+0.32}_{-0.03} \times 10^{10} M_{\odot}$  (Parkash et al. 2018).

In addition to the above parameter estimation of a boxcar model, we also use Bayesian Model Selection to compute the evidence ratio between a boxcar function and flat-line model (i.e. a null test of a constant value). We compute a Bayes factor of 50 between boxcar and flat-line model, which could be considered as ‘very strong’ evidence for the boxcar function hypothesis on the Jeffreys Scale. Assuming the boxcar model to be true, the probability of there being a positive H I mass is 99.8 per cent.

Within the limitations of the models employed, the Bayesian approach adds additional quantified rigour to the claimed detection. Deeper observations, preferably at high spatial and velocity resolution will be ultimately required to confirm this.

#### 4 GRAVITATIONALLY-LENSED H I

In addition to searching for H I in the clusters, we utilise the strong gravitational lensing properties of these massive clusters to search for magnified distant H I galaxies behind the clusters.

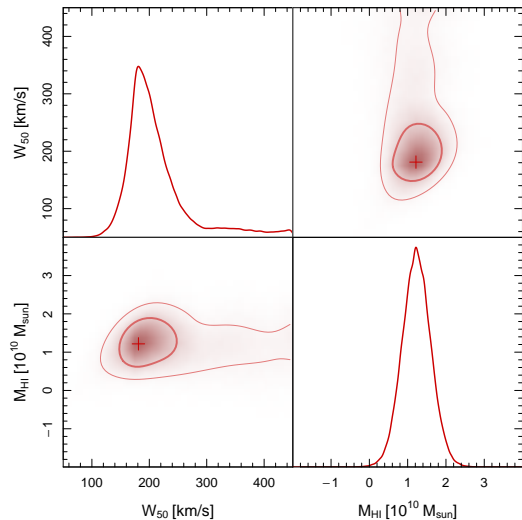


**Figure 10.** The posteriors for the Bayesian modelling of  $M_{\text{HI}}$  and  $w_{50}$ . The maximum likelihood solutions are indicated by the crosses. The thick and thin contours respectively show the 68 per cent and 95 per cent posterior probabilities.

#### 4.1 Predictions and Targeted Search

We modelled the predicted frequency-integrated H I flux  $S_{\text{HI}}$  [JyHz] of the 22 gravitationally lensed sources with known spectroscopic redshifts between each cluster and  $z = 0.5$ . As before, the integrated flux was estimated using Equation 2, assuming a velocity width of  $200 \text{ km s}^{-1}$  and the rms of the cubes. Assuming that the observed integrated H I flux scales linearly with magnification  $\mu$  (i.e. all sources are unresolved), we estimated the magnified integrated H I flux for each of these sources, assuming the CATS (Jauzac et al. 2014) lens model. The predicted results for the three HFF clusters are plotted in Fig. 11. From the predictions, we expect no detections greater than  $3\sigma$  for all three clusters. Only 12 of the 22 targets were investigated due to the limits of the cube frequency ranges and RFI contamination. Based on the coordinates and redshifts of targets with known spectroscopic redshifts, we detected no lensed H I emission for any of the clusters. This is consistent with the models in Blecher et al. (in prep.), who predict larger magnified H I masses for certain higher redshift targets beyond the frequency range of these L-band observations, the majority of which are redshifted into the UHF-band.

#### 4.2 Blind Search

We also performed a blind search for direct H I detection for lensed, but OIR faint, yet H I-massive objects, in the redshift range behind the clusters. We use the SoFIA software with the Smooth + Clip algorithm, as in Section 3.1, on the ‘background’ cubes. Continuum artefact filtering was also implemented. The source finding covered cosmological volumes of  $28\,815 \text{ Mpc}^3$  for Abell 2744,  $44\,775 \text{ Mpc}^3$  for Abell S1063, and  $31\,713 \text{ Mpc}^3$  for Abell 370. For all three clusters, no significant detections were found. Using the median cube rms (Table 3), we determine the  $5\sigma$  H I mass detection limits at  $z = 0.45$  to be  $M_{\text{HI}} = 3.89 \times 10^{10} \mu^{-1} M_{\odot}$ ,  $M_{\text{HI}} = 3.78 \times 10^{10} \mu^{-1} M_{\odot}$  and  $M_{\text{HI}} = 4.43 \times 10^{10} \mu^{-1} M_{\odot}$  for Abell 2744, Abell S1063 and Abell 370.



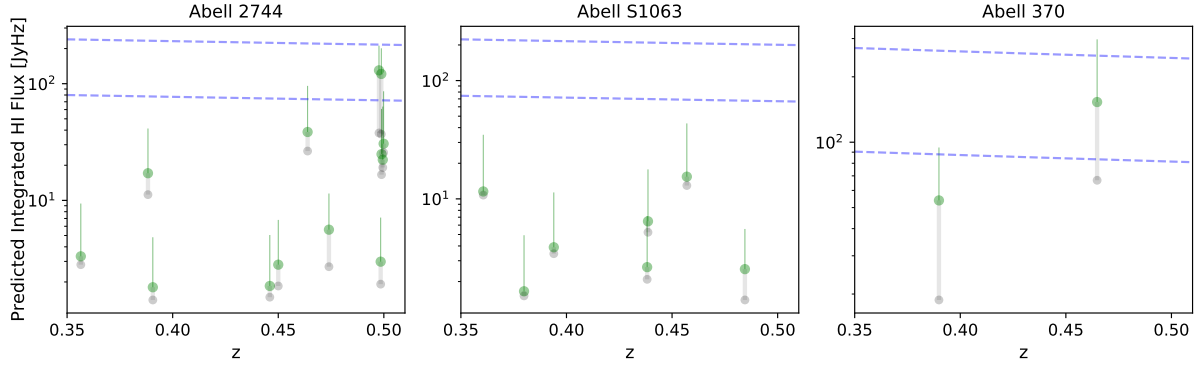


**Figure 11.** The predicted integrated flux (grey), and magnified integrated flux (green) of the objects lensed by the HFF clusters, as a function of redshift ( $z < 0.5$ ). For clarity, the grey bars connect the magnified and unmagnified points of the same source. We assume magnifications from CATS. The blue dashed lines show the  $1\sigma$  and  $3\sigma$  detection limits, and the upper error on the magnified flux are shown in green.

## 5 DISCUSSION

After stacking the galaxies with spectroscopic redshifts in each cluster (Section 3.2), we then stacked only the blue galaxies in Abell S1063 (Section 3.2.2) and found the average H I mass of blue galaxies in Abell S1063 to be significantly larger than expected. Elson et al. (2019) show that stacked H I masses are found to be overestimated in comparison to true H I results. Due to the low angular resolution H I cube in comparison with the angular extent of galaxies at high redshifts, the accuracy of stacked H I measurements can be greatly affected by source confusion (e.g. Delhaize et al. 2013). Using simulated H I data cubes, it is shown in Elson et al. (2016) that the overestimation of co-added H I mass, caused by source confusion, is more prevalent at lower angular resolution, as one would expect. Smoothing the cubes to poorer angular resolution has been shown to artificially boost the stacked H I signal (e.g. Fig. 6), but can simultaneously decrease the accuracy of the stacked H I mass. The small spatial (138 kpc) separation between the stacked sources (Fig. 7) has likely resulted in source confusion. In addition to this, as shown in Fig. 7, there are other visibly blue galaxies in the close vicinity of the stacked blue galaxies. These are excluded due to unknown spectroscopic redshifts, however their photometric redshifts suggest that they are cluster members and their H I flux could be contributing to the confusion. We do not see the characteristic emission peak broadening of this effect in Fig. 6 at our low SNR, as there are few stacked sources. Due to this, the measurement of  $M_{\text{HI}} = 1.22^{+0.38}_{-0.36} \times 10^{10} M_{\odot}$  cannot be taken as an accurate representation of the H I mass in Abell S1063. A detailed investigation and modelling of source confusion in this stacked measurement will be explored in future work with deeper observations and 32k correlator mode.

This is one of the few studies of the H I content of intermediate redshift galaxy clusters, which makes it difficult to make direct comparisons to the literature. However, we can compare to the stacked H I detection in Abell 370 by Lah et al. (2009). They make a  $2.7\sigma$  detection amounting to an average mass of  $M_{\text{HI}} = 4.8 \pm 1.8 \times 10^9 M_{\odot}$ , for data smoothed such that all sources are unresolved, spectra binned to  $\Delta V = 600 \text{ km s}^{-1}$ , and a sample consisting of 324 galaxies. This measurement is consistent with our upper H I mass limit for Abell 370. However, the sample of sources used in Lah et al. (2009) extends beyond the cluster into the area of the GMRT primary beam at 10% ( $58.5'$ ), significantly further than the public HFF sample (within  $2'$  of the cluster centre). A more appropriate comparison would be to the Lah et al. (2009) stack of red galaxies since 48 of our 49 can-

didate sources are classified as red, following the Lah et al. (2009) classification of  $(b - v) > 0.57$ . Here, they make what they claim to be a marginal  $1.2\sigma$  detection of  $M_{\text{HI}} = 2.6 \pm 2.1 \times 10^9 M_{\odot}$ , which is below the sensitivity limits of this experiment.

In this work, we assume the  $M_{*} - M_{\text{HI}}$  relation from Parkash et al. (2018), which is based on low-redshift, star-forming field galaxies, whereas our sample includes only intermediate-redshift cluster galaxies. This is reflected in the H I deficiencies calculated in Section 3.2.1. Further deep observations of H I in intermediate-redshift clusters will test the appropriateness of this relation and others (e.g. Catinella et al. 2010; Maddox et al. 2014), as well as their dependability and evolution with redshift and environment. Since galaxy clusters are dynamic environments, they host various processes that remove cold gas from galaxies. This is particularly prevalent in clusters with high X-ray luminosities, as found in Abell 2744, with  $L_{\text{X}} = 3.1 \times 10^{38} \text{ W}$  (Allen 1998). A modification to the  $M_{*} - M_{\text{HI}}$  relation would be needed to account for the H I deficiency in cluster galaxies to accurately predict their H I masses. Nonetheless, the mass limits probed and the stacked detection shows that this will now be possible at intermediate redshifts.

For all three clusters, there is an inconsistency between the observed rms values and the sensitivity limits obtained from the MeerKAT sensitivity calculator<sup>11</sup>, with the observed rms values  $\sim 55\%$  greater than the predicted values. A major contribution to this inconsistency is likely the bright and extended radio sources associated with these galaxy clusters, as well as an unfavourable Declination for Abell 370. Another contribution is the loss of data due to RFI, particularly for Abell 2744, and the MeerKAT correlator firmware issue. Alternatively, we can investigate the limitations of the calibration strategies used. All cluster measurement sets have  $\sim 20\%$  flagged visibilities in the considered frequency range of this work. This increases the rms noise by  $\sim 12\%$ , for continuum images. The increase of rms can also be attributed to the propagation of errors in the gain amplitude and flux scaling calibrations. The addition of direction-dependent calibration is expected to further improve the rms noise of the cubes, by mitigating the effect of the primary beam rotation, pointing errors and ionospheric issues. This will be explored in future works and deeper integrations on the HFF.

<sup>11</sup> <https://skaafrika.atlassian.net/servicedesk/customer/portals>

## 6 CONCLUSION

In this paper, we aimed to detect H I in Abell 2744, Abell S1063 and Abell 370, all massive galaxy clusters at  $0.3 < z < 0.5$ , using data from the MeerKAT Galaxy Cluster Legacy Survey. Through this, we aimed to achieve a better understanding of the H I content of galaxies in clusters at intermediate redshifts. No direct H I detections were made in the MeerKAT H I cluster cubes, and we determined  $3\sigma$  H I mass detection limits down to the knee of the HIMF.

We stacked the spectra of all sources with spectroscopic redshifts in the cube frequency ranges and found that the rms decreases approximately as expected, but detected no stacked emission in the central regions of all three clusters. We determined the stacked  $5\sigma$  H I mass limits to be  $M_{\text{HI}} = 2.89 \pm 0.21 \times 10^9 M_{\odot}$ ,  $M_{\text{HI}} = 2.05 \pm 0.04 \times 10^9 M_{\odot}$ , and  $M_{\text{HI}} = 4.89 \pm 0.19 \times 10^9 M_{\odot}$  for Abell 2744, Abell S1063 and Abell 370, respectively. We stacked the spectra of the five blue galaxies with spectroscopic redshifts in Abell S1063, and made a marginal  $3\sigma$  detection, at a velocity resolution of  $60 \text{ km s}^{-1}$ . We determined the average stacked H I mass to be  $M_{\text{HI}} = 1.22^{+0.38}_{-0.36} \times 10^{10} M_{\odot}$ . This is larger, by a factor of 10, than the predicted H I masses for the sources from the Parkash et al. (2018) relation, assuming this  $M_{*} - M_{\text{HI}}$  relation holds for galaxy clusters. Because of the large uncertainties for the predicted H I masses, we found that this large stacked H I mass is an overestimation, attributed to source confusion and possible environmental effects.

We also performed a search for lensed H I behind the HFF clusters Abell 2744, Abell S1063, and Abell 370, in the redshift range of  $z_{\text{cluster}} < z < 0.5$ , using data from the MeerKAT Galaxy Cluster Legacy Survey and make no direct detections. Despite the lack of lensed H I detections from these observations, the sensitivity of MeerKAT is sufficient to detect these lensed sources with a factor of 2 longer integration times. The MeerKAT UHF-band covers the redshift range of  $> 50$  additional lensed sources behind each cluster, which will be investigated with future observations.

These results demonstrate MeerKAT's capability of probing the intermediate redshift range, for high mass individual detections and statistical  $M_{\text{HI}}$  detections. MeerKAT is able to achieve these mass limits within early science observations, despite relatively short integration times for intermediate redshift observations. While not making direct detections, we have obtained mass limits that paint a highly promising picture for future MeerKAT observations, with longer integration times, of large samples of intermediate redshift galaxy clusters.

## ACKNOWLEDGEMENTS

The research of SR and RPD is supported by the South African Research Chairs Initiative (grant ID 77948) of the Department of Science and Innovation and National Research Foundation. SR and RPD acknowledge the financial assistance of the South African Radio Astronomy Observatory (SARAO) towards this research ([www.ska.ac.za](http://www.ska.ac.za)). IH acknowledges support from the UK Science and Technology Facilities Council [ST/N000919/1], and from the South African Radio Astronomy Observatory which is a facility of the National Research Foundation (NRF), an agency of the Department of Science and Innovation. DO is a recipient of an Australian Research Council Future Fellowship (FT190100083) funded by the Australian Government. The MeerKAT telescope is operated by the South African Radio Astronomy Observatory, which is a facility of the National Research Foundation, an agency of the Department of Science and Innovation. We acknowledge use of the Inter-University

Institute for Data Intensive Astronomy (IDIA) data intensive research cloud for data processing. IDIA is a South African university partnership involving the University of Cape Town, the University of Pretoria and the University of the Western Cape. The authors acknowledge the Centre for High Performance Computing (CHPC), South Africa, for providing computational resources to this research project. This work has made use of the Cube Analysis and Rendering Tool for Astronomy (CARTA; Comrie et al. 2021). This work is based on data and catalogue products from HFF-DeepSpace, funded by the National Science Foundation and Space Telescope Science Institute (operated by the Association of Universities for Research in Astronomy, Inc., under NASA contract NAS5-26555).

## DATA AVAILABILITY

The radio data used in this analysis are publicly available through the SARAO archive at <https://archive.sarao.ac.za/> under proposal ID SSV-20180624-FC-01. Data and catalogue products from HFF-DeepSpace (Shipley et al. 2018) are publicly available at <http://cosmos.phy.tufts.edu/~danilo/HFF/Download.html>. Calibrated images and spectra may be made available upon reasonable request.

## REFERENCES

- Allen S. W., 1998, *MNRAS*, 296, 392–406  
 Bera A., Kanekar N., Chengalur J. N., Bagla J. S., 2019, *ApJ*, 882, L7  
 Bialas D., Lisker T., Olczak C., Spurzem R., Kotulla R., 2015, *A&A*, 576, A103  
 Blecher T., Deane R., Heywood I., Obreschkow D., 2019, *MNRAS*, 484, 3681–3690  
 Blyth S., et al., 2016, in MeerKAT Science: On the Pathway to the SKA. p. 4  
 Broeils A. H., Rhee M. H., 1997, *A&A*, 324, 877  
 Brown T., Catinella B., Cortese L., Kilborn V., Haynes M. P., Giovanelli R., 2015, *MNRAS*, 452, 2479–2489  
 Brown T., et al., 2016, *MNRAS*, 466, 1275–1289  
 Carilli C., Walter F., 2013, *ARA&A*, 51, 105–161  
 Catinella B., et al., 2010, *MNRAS*, 403, 683–708  
 Chowdhury A., Kanekar N., Chengalur J. N., Sethi S., Dwarakanath K. S., 2020, *Nature*, 586, 369  
 Comrie A., et al., 2021, CARTA: The Cube Analysis and Rendering Tool for Astronomy, doi:10.5281/zenodo.4905459, <https://doi.org/10.5281/zenodo.4905459>  
 Cortese L., Catinella B., Boissier S., Boselli A., Heinis S., 2011, *MNRAS*, 415, 1797–1806  
 Deane R. P., Obreschkow D., Heywood I., 2015, *MNRAS: Letters*, 452, L49–L53  
 Delhaize J., Meyer M. J., Staveley-Smith L., Boyle B. J., 2013, *MNRAS*, 433, 1398–1410  
 Deshev B., Haines C., Hwang H. S., Finoguenov A., Taylor R., Orlitova I., Einasto M., Ziegler B., 2020, *A&A*, 638, A126  
 Dressler A., et al., 1997, *ApJ*, 490, 577–591  
 Dressler A., Smail I., Poggianti B. M., Butcher H., Couch W. J., Ellis R. S., Oemler Jr. A., 1999, *ApJ Supplement Series*, 122, 51–80  
 Dénes H., Kilborn V. A., Koribalski B. S., Wong O. I., 2015, *MNRAS*, 455, 1294–1308  
 Elson E. C., Blyth S. L., Baker A. J., 2016, *MNRAS*, 460, 4366–4381  
 Elson E. C., Baker A. J., Blyth S. L., 2019, *MNRAS*, 486, 4894–4903  
 Fernández X., et al., 2016, *ApJ*, 824, L1  
 Gavazzi G., Consolandi G., Gutierrez M. L., Boselli A., Yoshida M., 2018, *A&A*, 618, A130  
 Gunn J. E., Gott J. R., 1972, *ApJ*, 176, 1  
 Haynes M. P., Giovanelli R., 1984, *AJ*, 89, 758

- Healy J., Blyth S.-L., Elson E., van Driel W., Butcher Z., Schneider S., Lehnert M. D., Minchin R., 2019, *MNRAS*, 487, 4901–4938
- Healy J., et al., 2021, *A&A*, 650, A76
- Hess K. M., Wilcots E. M., 2013, *AJ*, 146, 124
- Heywood I., 2020, *oxkat*: Semi-automated imaging of MeerKAT observations (ascl:2009.003)
- Hu W., et al., 2019, *MNRAS*, 489, 1619–1632
- Hunt L. R., Pisano D. J., Edell S., 2016, *AJ*, 152, 30
- Jaffé Y. L., Poggianti B. M., Verheijen M. A. W., Deshev B. Z., van Gorkom J. H., 2013, *MNRAS*, 431, 2111–2125
- Jaffé Y. L., Smith R., Candlish G. N., Poggianti B. M., Sheen Y.-K., Verheijen M. A. W., 2015, *MNRAS*, 448, 1715–1728
- Jarvis M. J., et al., 2017, The MeerKAT International GHz Tiered Extragalactic Exploration (MIGHTEE) Survey (arXiv:1709.01901)
- Jauzac M., et al., 2014, *MNRAS*, 443, 1549
- Joshi G. D., Pillepich A., Nelson D., Marinacci F., Springel V., Rodriguez-Gomez V., Vogelsberger M., Hernquist L., 2020, *MNRAS*, 496, 2673–2703
- Józsa G. I. G., et al., 2020, CARACal: Containerized Automated Radio Astronomy Calibration pipeline (ascl:2006.014)
- Kanekar N., Sethi S., Dwarakanath K. S., 2016, *ApJ*, 818, L28
- Karman W., et al., 2015, *A&A*, 574, A11
- Kenyon J. S., Smirnov O. M., Grobler T. L., Perkins S. J., 2018, *MNRAS*, 478, 2399
- Kereš D., Katz N., Weinberg D. H., Dave R., 2005, *MNRAS*, 363, 2–28
- Kneib J.-P., Natarajan P., 2011, *A&ARv*, 19
- Knowles K., et al., 2021, The MeerKAT Galaxy Cluster Legacy Survey I. Survey Overview and Highlights (arXiv:2111.05673)
- Lagattuta D. J., et al., 2017, *MNRAS*, 469, 3946–3964
- Lah P., et al., 2009, *MNRAS*, 399, 1447–1470
- Lee-Waddell K., et al., 2017, *MNRAS*, 474, 1108–1115
- Leroy A. K., Walter F., Brinks E., Bigiel F., de Blok W. J. G., Madore B., Thornley M. D., 2008, *AJ*, 136, 2782–2845
- Li J., Obreschkow D., Lagos C., Cortese L., Welker C., Džudžar R., 2020, *MNRAS*, 493, 5024–5037
- Lotz J. M., et al., 2017, *ApJ*, 837, 97
- Ma C., Ebeling H., Donovan D., Barrett E., 2008, *ApJ*, 684, 160–176
- Maddox N., Hess K. M., Obreschkow D., Jarvis M. J., Blyth S.-L., 2014, *MNRAS*, 447, 1610–1617
- Mahler G., et al., 2017, *MNRAS*, 473, 663–692
- Makhathini S., 2018, PhD thesis, Rhodes University, Drostdy Rd, Grahamstown, 6139, Eastern Cape, South Africa
- Mauch T., et al., 2020, *ApJ*, 888, 61
- McMullin J. P., Waters B., Schiebel D., Young W., Golap K., 2007, in Shaw R. A., Hill F., Bell D. J., eds, *Astronomical Society of the Pacific Conference Series Vol. 376, Astronomical Data Analysis Software and Systems XVI*. p. 127
- Meyer M., Robotham A., Obreschkow D., Westmeier T., Duffy A. R., Staveley-Smith L., 2017, *Publications of the Astronomical Society of Australia*, 34
- Moore B., Lake G., Katz N., 1998, *ApJ*, 495, 139
- Noordam J. E., Smirnov O. M., 2010, *A&A*, 524, A61
- Obreschkow D., Rawlings S., 2009, *ApJ*, 696, L129–L132
- Odekon M. C., et al., 2016, *ApJ*, 824, 110
- Offringa A. R., 2010, *AOFlogger*: RFI Software (ascl:1010.017)
- Offringa A. R., et al., 2014, *MNRAS*, 444, 606
- Oosterloo T., van Gorkom J., 2005, *A&A*, 437, L19–L22
- Owers M. S., Randall S. W., Nulsen P. E. J., Couch W. J., David L. P., Kempner J. C., 2011, *ApJ*, 728, 27
- Parkash V., Brown M. J. I., Jarrett T. H., Bonne N. J., 2018, *ApJ*, 864, 40
- Planck Collaboration et al., 2015, *A&A*, 594, A13
- Poggianti B. M., Bridges T. J., Komiyama Y., Yagi M., Carter D., Mobasher B., Okamura S., Kashikawa N., 2004, *ApJ*, 601, 197–213
- Péroux C., Howk J. C., 2020, *ARA&A*, 58, 363–406
- Ramatsoku M., et al., 2020, *A&A*, 640, A22
- Rhee J., Zwaan M. A., Briggs F. H., Chengalur J. N., Lah P., Oosterloo T., Hulst T. v. d., 2013, *MNRAS*, 435, 2693–2706
- Richard J., Kneib J.-P., Limousin M., Edge A., Jullo E., 2009, *MNRAS: Letters*, 402, L44–L48
- Roediger E., Brüggem M., 2007, *MNRAS*, 380, 1399–1408
- Salerno J. M., et al., 2020, *MNRAS*, 493, 4950–4959
- Saponara J., Koribalski B. S., Benaglia P., Fernández López M., 2017, *MNRAS*, 473, 3358–3366
- Serra P., et al., 2012, *MNRAS*, 422, 1835–1862
- Serra P., et al., 2015, *MNRAS*, 448, 1922–1929
- Shipley H. V., et al., 2018, *ApJ Supplement Series*, 235, 14
- Solanes J., Manrique A., García-Gómez C., González-Casado G., Giovanelli R., Haynes M., 2001, *ApJ*, 548, 97–113
- Sorgho A., Hess K., Carignan C., Oosterloo T. A., 2017, *MNRAS*, 464, 530
- Verheijen M. A. W., 2004, *Proceedings of the International Astronomical Union*, 2004
- Verheijen M., van Gorkom J. H., Szomoru A., Dwarakanath K. S., Poggianti B. M., Schiminovich D., 2007, *ApJ*, 668, L9–L13
- Vollmer B., Soida M., Beck R., Chung A., Urbanik M., Chyży K. T., Otmianowska-Mazur K., Kenney J. D. P., 2013, *A&A*, 553, A116
- Wang J., Koribalski B. S., Serra P., van der Hulst T., Roychowdhury S., Kamphuis P., N. Chengalur J., 2016, *MNRAS*, 460, 2143–2151
- Wetzel A. R., Tinker J. L., Conroy C., van den Bosch F. C., 2013, *MNRAS*, 432, 336–358
- Williamson R., et al., 2011, *ApJ*, 738, 139
- van der Wel A., Bell E. F., Holden B. P., Skibba R. A., Rix H.-W., 2010, *ApJ*, 714, 1779–1788

This paper has been typeset from a  $\text{\TeX}/\text{\LaTeX}$  file prepared by the author.